Journal of Materials Research and Technology 29 (2024) 4597–4606

Contents lists available at ScienceDirect

Journal of Materials Research and Technology

journal homepage: www.elsevier.com/locate/jmrt

3D printing of potassium sodium niobate by binder jetting: Printing parameters optimisation and correlation to final porosity

Francesco Bertolini [a,*], Marco Mariani [a], Elisa Mercadelli [b], Carlo Baldisserri [b], Carmen Galassi [a,b], Claudio Capiani [b], Raffaele Ardito [c], Nora Lecis [a]

[a] Department of Mechanical Engineering, Politecnico di Milano, Milano, 20156, Italy
[b] National Research Council of Italy, Institute of Science, Technology and Sustainability for Ceramics (CNR-ISSMC, Former ISTEC), Faenza, 48018, Italy
[c] Department of Civil and Environmental Engineering, Politecnico di Milano, Milano, 20133, Italy

ARTICLE INFO

Handling Editor: Prof. M Meyers

Keywords:
Binder jetting
Additive manufacturing
Porous piezoceramic
Potassium sodium niobate
Design of experiment
Taguchi method

ABSTRACT

Binder Jetting (BJT) is a non-fusion-based Additive Manufacturing (AM) technique. It consists of the selective deposition of a liquid binder to join powder particles, thereby enabling the creation of near-net-shaped parts.

In this study, the main printing parameters correlated to the binder distribution and infiltration (binder saturation, binder set time, drying time, and target bed temperature) were optimised to improve the precision of green parts printed with potassium sodium niobate (KNN) powder. The optimisation procedure was conducted using the Taguchi statistical method. An L_9 orthogonal array with four factors of control at three levels each was employed. The analysis showed that the drying time had the greatest influence on the precision of green parts, followed by binder saturation and target bed temperature. Binder set time did not seem to affect the results.

Dimensional analysis, microstructural and piezoelectric characterisation of parts densified by pressureless sintering were conducted. The highest average relative density exceeded 80% for the specimens printed with the lower binder saturation. Piezoelectric properties exhibit more complex behaviour. The prolonged infiltration of larger binder volumes is correlated to higher g_{33}, thus FOM_h and FOM_{33}, and lower values for ε_{33}^T. On the other hand, d_{33} does not display a specific dependence on density or printing parameters.

The results of this study indicate that BJT can be used to fabricate high-precision KNN components with good piezoelectric properties. The optimisation of printing parameters is essential to achieve the desired results.

1. Introduction

Additive manufacturing (AM) of piezoceramics has gained significant interest in recent years, particularly in the fields of energy harvesting and electronic device production. This technology allows the creation of complex parts with a high degree of precision and tailoring the piezoelectric properties, thus amplifying, suppressing, or reversing the device's response [1]. The most common techniques used in the production of piezoceramics are Vat-Photopolymerisation (VPP), Selective Laser Sintering (SLS), Material Extrusion (MEX), and Binder Jetting (BJT) [1,2].

BJT utilises a liquid polymeric binder to bond powder particles and creates green parts. It relies on a powder bed to sustain the components during the process, obviating the need for support structures. After printing, the parts must undergo curing in an oven to consolidate the polymer, enabling handling and removal of the recoverable excess powder. Finally, densification is achieved through a sintering step.

There are numerous parameters that can be modified during the printing. Some affect how the powder is spread and compacted while other are related to the deposition and drying of the binder.

The main advantages of BJT include the ability to work with different materials, the limited amount of binder needed per unit, the scalability for large-volume production series, the high throughput with a cost-effective process, and the ability to operate at room temperature [3–6].

Piezoelectric ceramics enable the conversion of electrical and mechanical signals, making them versatile for various applications such as sensors, actuators, and transducers [7]. In particular, piezoelectric materials enable the implementation of energy harvesting procedures, for the conversion of mechanical energy (e.g. vibrations) into electrical energy, to possibly feed ultra-low-power sensors [8]. In recent times, many efforts have been devoted to the application of metamaterials to

* Corresponding author.
E-mail address: francesco.bertolini@polimi.it (F. Bertolini).

https://doi.org/10.1016/j.jmrt.2024.02.145
Received 14 November 2023; Received in revised form 12 February 2024; Accepted 19 February 2024
Available online 23 February 2024

Table 1
Factors and levels used in the Taguchi Design (*BS* = binder saturation, *BST* = binder set time, *DT* = drying time, *TBT* = target bed temperature).

	BS [%]	*BST* [s]	*DT* [s]	*TBT* [°C]
Level 1	110	6	6	40
Level 2	130	10	10	50
Level 3	150	14	14	60

Table 2
$L_9(3^4)$ Taguchi Design; selected values of the parameters (*BS* = binder saturation, *BST* = binder set time, *DT* = drying time, *TBT* = target bed temperature).

	BS [%]	*BST* [s]	*DT* [s]	*TBT* [°C]
Run 1	110	6	6	40
Run 2	110	10	10	50
Run 3	110	14	14	60
Run 4	130	6	10	60
Run 5	130	10	14	40
Run 6	130	14	6	50
Run 7	150	6	14	50
Run 8	150	10	6	60
Run 9	150	14	10	40

enhance the performances of piezoelectric energy harvesting [9,10], with the definition of non-trivial geometry for the devices. The adoption of AM techniques is of paramount importance for achieving the general shape of these materials and it could potentially lead to a substantial reduction in production costs, since machining operations to produce complex shapes account for more than 70% of the total expenditure in ceramics manufacturing [11]. Additionally, AM offers the advantage of minimising material waste and facilitating the realisation of complex geometries, ultimately aiming to enhance functional properties [2].

Among piezoelectric ceramics, the most used is lead zirconate titanate ($Pb[Zr_xTi_{1-x}]O_3$) or PZT, due to its excellent properties and flexibility in terms of compositional modification. However, there has been an increasing focus on environmentally friendly materials, especially as European regulations have become more stringent regarding hazardous substances like lead [12]. In 2006 the European Parliament adopted the directives Waste Electrical and Electronic Equipment (WEEE) and Restriction of the use of certain Hazardous Substances in electrical and electronic equipment (RoHS) [13,14], limiting the maximum allowed concentration of lead at 0.1 wt% in all electrical and electronic products (except for piezoelectrics). Similar regulations are present or planned all over the world [15–21].

Potassium sodium niobate (K_xNa_{1-x}) NbO_3 (KNN) and its derivative materials have emerged as promising lead-free alternatives to PZT. They are characterised by high Curie temperature (~420 °C), high dielectric constant (~600) and moderate piezoelectric strain constant (d_{33} = 80–120 pC N^{-1}). In recent years it has been one of the most extensively investigated piezoelectric systems with nearly half of the publications in the field of lead-free piezoceramics focusing on alkali-niobium-based materials in the time range 2004–2014 [22].

Currently, there are limited feasibility studies on BJT of piezoceramics, especially in the case of KNN, making it a highly compelling area for further research [23–28]. The results are very different depending on the material used both in terms of density and piezoelectric properties. However promising results have been obtained suggesting a possible route for BJT to produce porous piezoceramics.

The complexity arising from the numerous parameters and the

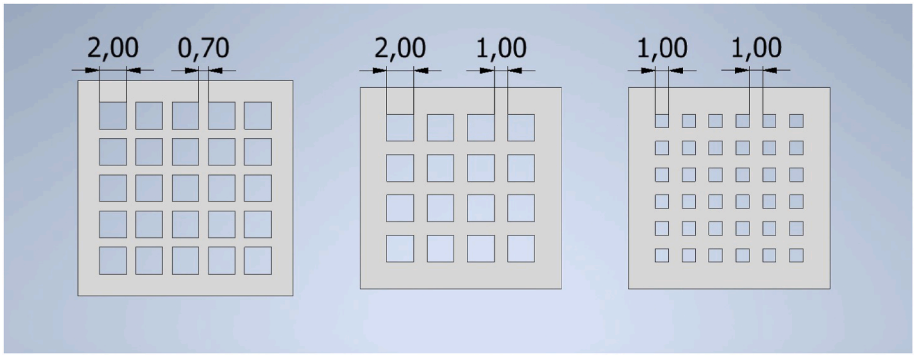

Fig. 1. Front view of the CAD file of the 3 grids. All measurements are in mm.

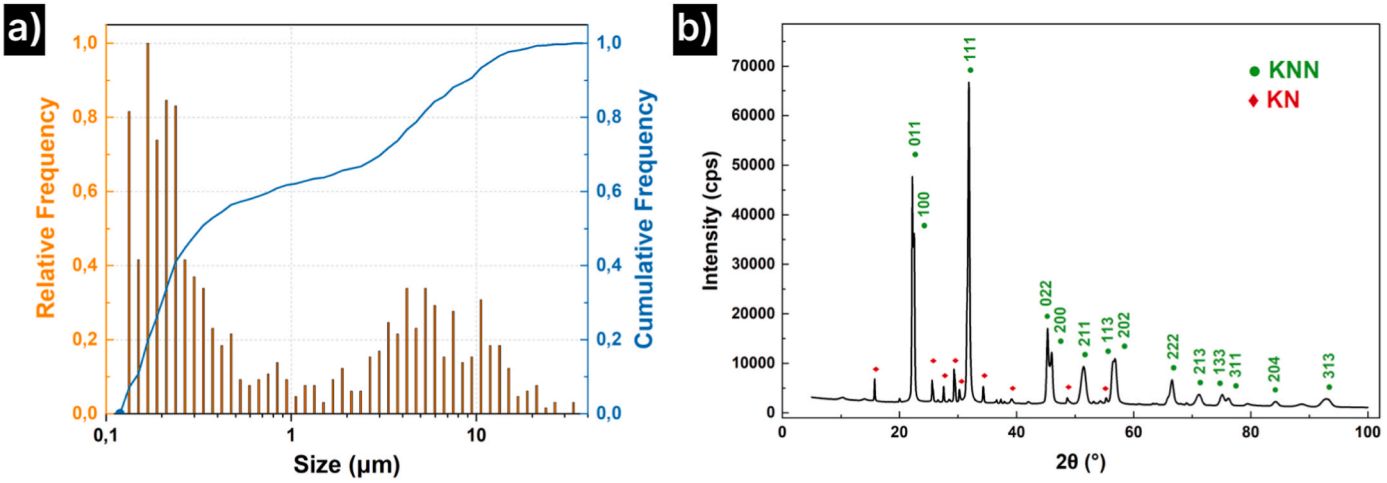

Fig. 2. Relative and cumulative frequency distributions (a) and XRD diffractogram (b). Crystallographic planes are marked only for the main phase (KNN).

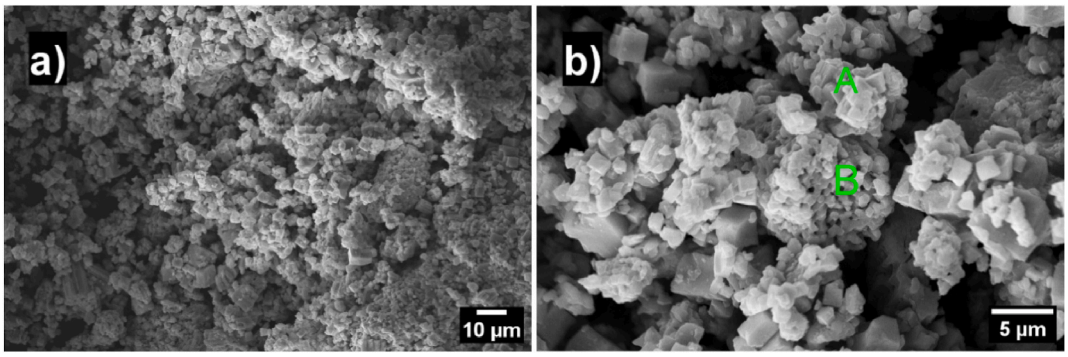

Fig. 3. SEM images of KNN powder at different magnifications. In (b) A is the KNN phase and B is the KN phase, as determined by EDX analysis.

Table 3
Results of EDX analysis of Fig. 3. The results are expressed in atomic %.

	% Na	% K	% Nb
Spectrum A (KNN)	26.09	23.12	50.78
Spectrum B (KN)	5.59	18.46	75.95

Table 4
Dimensional analyses of the green bodies.

	σ_d [mm]	σ_t [mm]	ρ_{rel} [%]
Run 1	0.23	0.07	36.2
Run 2	0.18	0.11	35.4
Run 3	0.06	0.07	37.9
Run 4	0.06	0.12	39.8
Run 5	0.04	0.04	39.8
Run 6	0.14	0.11	40.7
Run 7	0.11	0.06	38.9
Run 8	0.14	0.08	40.3
Run 9	0.21	0.07	40.6

diverse range of potential configurations made necessary the use of a tool to assess the impacts of these various parameters on the outcomes and to streamline the experimental process. The Design of Experiment (DoE) is a statistical method used to systematically classify and quantify cause-and-effect relationships between variables and the results of a given process or phenomenon [29]. The Taguchi Design (TD) is a particular one that exploits an orthogonal array to reduce the number of experimental runs with respect to a Full Factorial Design (FFD), which would have considered all the possible combinations between the parameters while constituting a balanced experiment [30].

The aim of this work was to optimise the values of the binder-related printing parameters to obtain precise green parts by minimising the standard deviation in diameter and thickness measurements. The microstructure of the sintered parts was characterised as well, and the piezoelectric properties were analysed to understand the influence of porosity on the component performance.

2. Materials and methods

2.1. Materials

In this study potassium sodium niobate ($K_{0.5}Na_{0.5}NbO_3$) powder supplied by AMERICAN ELEMENTS® (USA) was selected as feedstock. During sintering, the samples were embedded in KNN powder with an alkali excess of 2 wt%, produced by CNR-ISSMC (Italy), to compensate for the elements evaporation. The aqueous-based commercial product AquaFuse® (previously known as BA005) by ExOne (USA) was used as the liquid binder for the printing process.

2.2. Printing and post-processing

Before printing, the powder was pre-heated at 60 °C for 1 h in air to remove adsorbed humidity and improve flowability. All specimens were manufactured with an Innovent+ 3D printer from ExOne (USA). The parameters selected as factors were binder saturation (*BS*), binder set time (*BST*), drying time (*DT*), and target bed temperature (*TBT*). *BS* is defined as the ratio of the volume of binder deposited to the pore volume of the powder bed in each layer, that was decided to fix at 60%. Therefore, *BS* might not accurately reflect the actual saturation level in the powder bed. Consequently, although higher-than-100% saturation level would potentially exert negative impact to the green part quality (e.g. over-permeation, inadequate in-process part strength), the high values of binder saturation used in the DoE should not be interpreted with their literal values. *BST* is the time between the binder deposition and the drying step that allows the binder to soak into the powder bed before drying. *DT* is the time the heater passes on the powder bed. The range have been decided starting from the company indication and from literature [23–28].

It was decided to have 3 levels per factor, as outlined in Table 1. Noise factors were omitted from consideration since the laboratory environment was controlled; all the powder used originated from the same batch, and all operations were performed by a single operator employing a single machine.

The layer thickness was fixed at 50 μm, while the other printing parameters regarding powder deposition, spreading, and compacting

Fig. 4. Details of samples displaying printing defects: (a) plane slippage; (b), (c) bleeding.

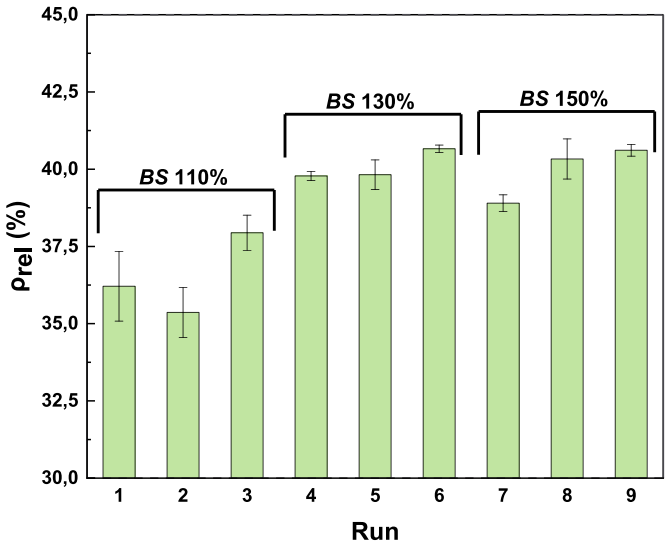

Fig. 5. Relative density values for green parts for each run.

Table 5
Results of first ANOVA of the mean of σ_t, σ_d.

	DF	Seq SS	Adj SS	Adj MS	F	P
BS	2	0.001882	0.001882	0.000941	*	*
BST	2	0.000271	0.000271	0.000136	*	*
DT	2	0.011104	0.011104	0.005552	*	*
TBT	2	0.002143	0.002143	0.001072	*	*
Residual Error	0	*	*	*		
Total	8	0.015401				

Table 6
Results of second ANOVA of the mean of σ_t, σ_d.

	DF	Seq SS	Adj SS	Adj MS	F	P
BS	2	0.001882	0.001882	0.000941	6.94	0.126
DT	2	0.011104	0.011104	0.005552	40.94	0.024
TBT	2	0.002143	0.002143	0.001072	7.90	0.112
Residual Error	2	0.000271	0.000271	0.000136		
Total	8	0.015401				

were adjusted to accommodate the behaviour of the powder and to ensure the creation of a compact powder bed. The experimental design followed the Taguchi $L_9(3^4)$ method, with four control factors at three levels each, resulting in a total of 9 runs (Table 2) [29]. The sample geometry was a disk with a diameter of 15.73 mm and a thickness of 2.475 mm; three disks were produced per run.

The results were analysed through Minitab software, utilizing a "smaller-the-better" approach in Level Average Analysis (LAA) for the standard deviations of diameter and thickness measurements (σ_t, σ_d). The software also provided the results of the ANOVA. Upon determination of the optimal levels for each parameter, the geometric design capabilities of the printing processes were initially assessed by conducting subsequent prints with varying wall thicknesses (0.7 or 1 mm) and/or hole dimensions (1 or 2 mm) in a grid pattern, as illustrated in Fig. 1.

The curing process was conducted at 180 °C for 6 h in air to achieve the polymerisation of the monomer dissolved within the binder and the evaporation of residual solvents. De-powdering was accomplished through the use of brushes and manual air blowing.

The debinding procedure was integrated into the sintering phase, which consolidated the samples. The thermal cycle involved heating in air to 470 °C for 2 h for polymer burnout and then to 1130 °C for 2 h for sintering, in the presence of atmospheric powder. The two steps were carried out consecutively without cooling. The heating rate was 2.5 °C min^{-1} and the cooling followed the natural profile of the oven.

2.3. Characterisations

The size distribution and mean size of the particulate feedstock were determined by optical granulometry (ASTM E2651-19) with a Malvern Morphologi 4 (UK) granulometer which allowed calculating the cumulative and relative frequency curves of the number-based size distribution with a logarithmic binning.

Powder morphology was determined by field emission scanning electron microscopy (FE-SEM, ZEISS Sigma 500, Germany), while the qualitative elemental composition was determined by energy dispersive X-ray (EDX).

Phases identification was performed with X-ray diffraction (XRD), over the $20° \leq 2\theta \leq 80°$ range (step size 0.02°) at a scanning rate of 1° min^{-1} with Cu-Kα radiation (λ = 1.5406 Å), in a Smartlab SE Rigaku (Japan) diffractometer.

The green and sintered densities were evaluated by the geometrical method. The green density is referred to the density of the printed sample after the depowdering step, so it includes the binder weight in the mass calculation [31,32]. Relative density values were calculated with reference to the theoretical density of 4.50 g cm^{-3} [33]. Both fracture surfaces and polished sections of the sintered samples were investigated by FE-SEM and EDX analysis.

The piezoelectric properties were determined on samples prepared by geometrical regularisation through manual lapping on emery paper, to obtain thin disks (d ~ 12 mm, s ~ 1 mm). 160 nm-thick silver electrodes were sputtered onto the two circular faces of the disks with a Quorum Q150T ES (UK) plasma coater. Dielectric and piezoelectric properties were evaluated after the poling process (3 kV mm^{-1} at 120 °C for 40 min) by acquiring their room-temperature piezoresonance spectra with an HP 4194A (USA) impedance analyser, by detecting resonance and antiresonance frequencies over the 100 Hz–40 MHz range. Room-temperature capacitance and loss tangent were measured at 1 kHz with the same instrument. d_{33} piezoelectric charge coefficient constants were measured using a Sinocera S5865 (China) d_{33}-m. Dielectric and piezoelectric constants were calculated from piezoresonance primary data using a MATLAB (MathWorks, USA) routine according to IEEE standards for piezoelectric measurements [34].

3. Results and discussion

3.1. Morphological and microstructural characterization

3.1.1. KNN powder

The granulometric analysis (Fig. 2a) and the scanning electron microscopy (SEM) examinations (Fig. 3) reveal that the powder consists of irregularly shaped micrometric and sub-micrometric cuboid particles, displaying a bimodal distribution pattern.

The powder exhibits a broad size distribution, ranging from approximately 0.1 μm to 35 μm. Predominantly, the particle size ranges from hundreds of nanometres to a few micrometres, as indicated by the change in slope observed in the cumulative frequency curve. Nonetheless, larger fragments and agglomerates can be observed in the 5–20 μm size range. This bimodal distribution is expected to enhance the packing density of the powder, with the smaller particles filling the interstitial spaces between the larger ones, even though optimal results could be achieved only with the primary fraction corresponding to that of the coarse particles [35].

The results of EDX analysis (Table 3) and XRD analysis (Fig. 2b) consistently confirm the presence of a second phase characterized by a high content of niobium (Nb) and potassium (K), likely corresponding to $K_6Nb_{10.88}O_{30}$. This second phase is identifiable by its irregular morphology and the visibly prominent rough-grain facets observed in

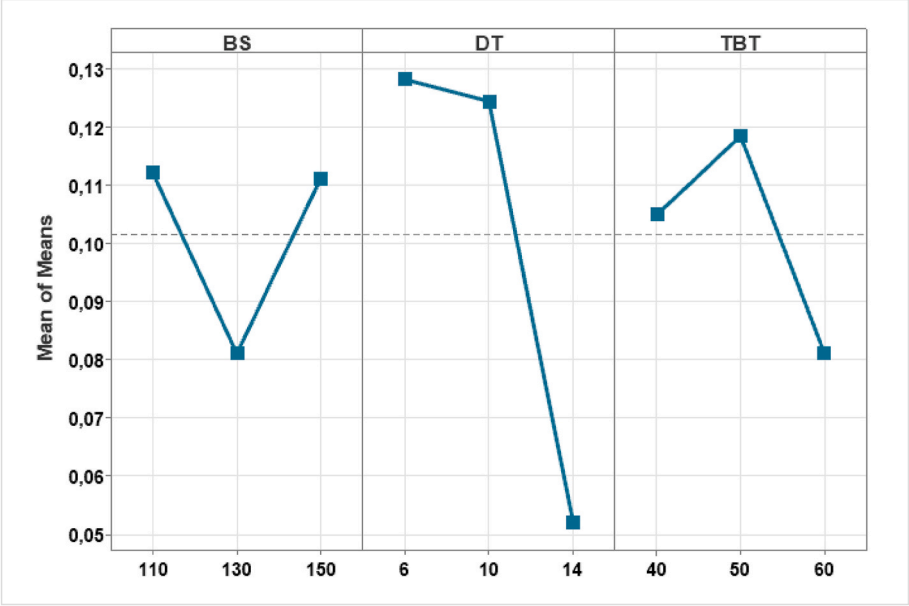

Fig. 6. Response table for the mean of σ_t,σ_d.

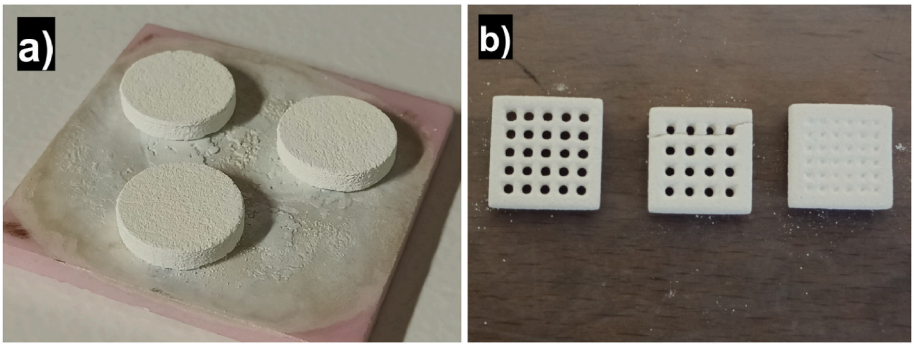

Fig. 7. Green parts of the confirmation run (a). Green grid-shaped parts after de-powdering (b).

Table 7
Results of dimensional analysis of confirmation run.

	σ_d [mm]	σ_t [mm]	ρ_{rel} [%]
Run C	0.03	0.02	39.2

the SEM images.

3.1.2. *Green parts*

The green parts exhibit appreciable accuracy in terms of diameter with respect to the CAD file and display acceptable precision across various runs. However, there is a noticeable disparity in the thickness, both in terms of accuracy and precision. The average diameter and thickness relative to the CAD file measures are 104 ± 2% and 130 ±

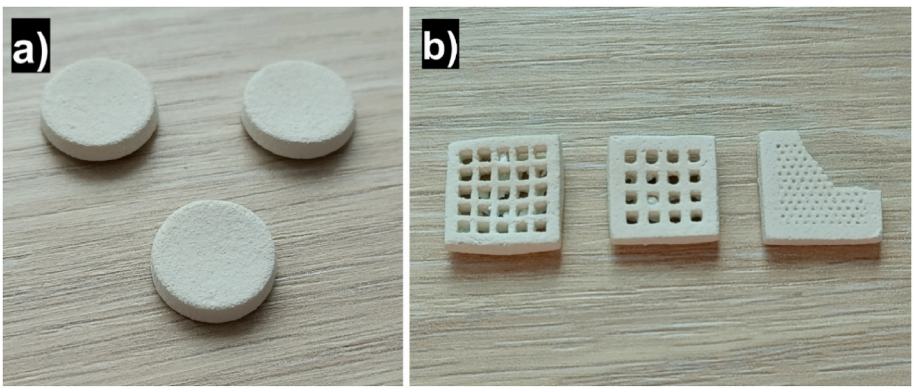

Fig. 8. Sintered parts after the removal from the furnace (a). Grid samples after sintering (b). The piece on the right was broken during de-powdering.

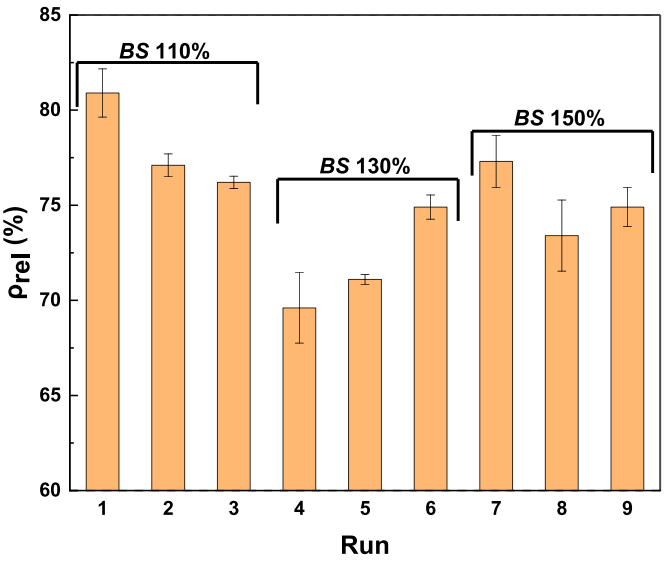

Fig. 9. Relative density values for sintered parts for each run.

13%, respectively. This observation underscores the reliability and accuracy of the process in the xy-plane, in comparison to the z-direction [36].

Furthermore, the analysis suggests that the samples printed with *BS* = 130% (runs 4–6) yield the best results in terms of accuracy and precision of diameter, whereas higher or lower values of *BS* tend to result in inconsistencies (Table 4). Low *BS* samples show some slippage of planes, probably because the layers did not have enough adherence due to incomplete binder imbibition (Fig. 4a). In contrast, high *BS* samples manifest bleeding phenomena, where excess binder spreads laterally, jeopardising the component's shape (Fig. 4b and c).

The relative densities are low when compared to the packing density achievable through conventional manufacturing processes. The values vary slightly, ranging from 35.4% to 40.7%, with an average of 38.8 ± 1.8%.

It is worth noting that there is an observable correlation with the binder saturation (*BS*) value (Fig. 5). A higher amount of deposited binder helps to fill the powder bed porosity, contributing to an increased density of the samples. The values are higher than the one found in the only other reference dealing with BJT of KNN (ρ_{rel} = 35%) [23], underlining that this specific feedstock provides better packing during deposition on the building platform.

The Taguchi method was employed to enhance geometric precision by minimising the standard deviations of thickness and diameter among different samples produced under the same printing conditions. The ultimate goal was to achieve green parts with maximum precision, ensuring repeatability and minimal standard deviations. This, in turn,

Table 8
Results of EDX analysis of Fig. 10d. The results are expressed in atomic %.

	%Na	%K	%Nb
Spectrum A (KN)	4.71	28.8	66.49
Spectrum B (KNN)	20.22	27.08	52.7

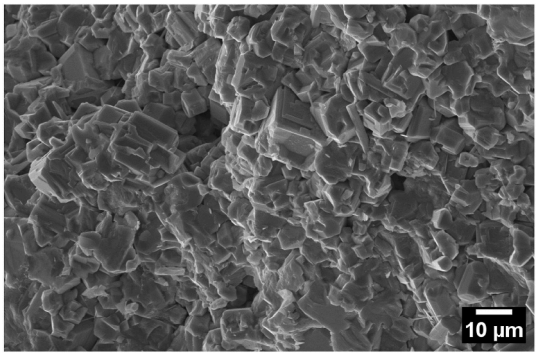

Fig. 11. SEM image of the fracture surface of a sintered sample.

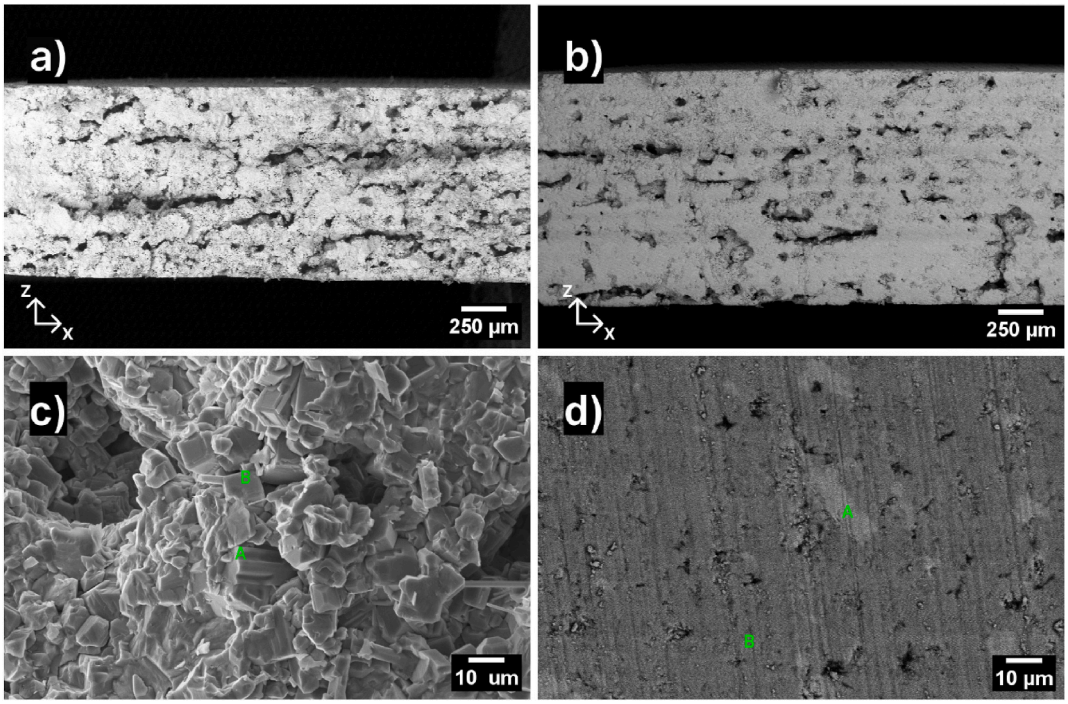

Fig. 10. SEM images of the sintered sample, fracture surface (a), (c) and polished surface (b), (d) at different magnifications. The image (d) is in BSEs configuration and phases A (KN) and B (KNN) are detectable by different brightness.

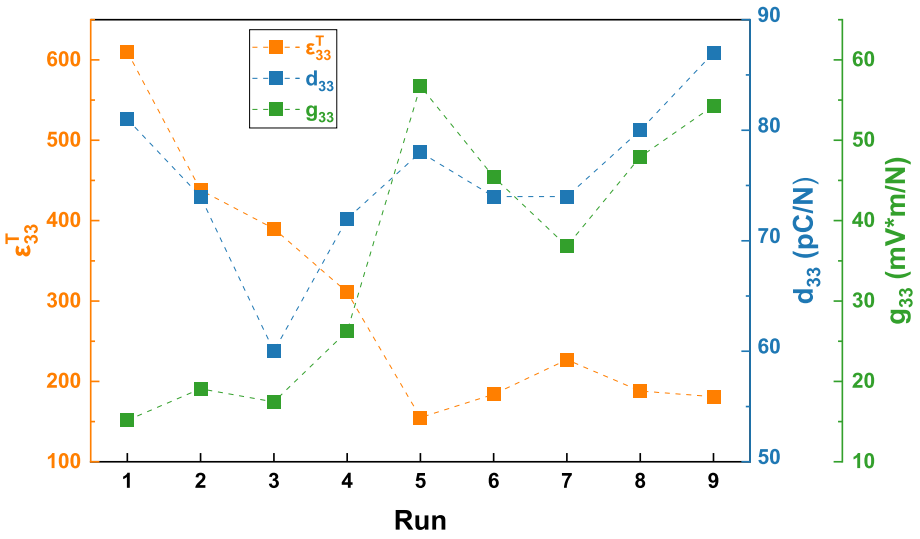

Fig. 12. Comparison of piezoelectric properties (d_{33}, g_{33} and e_{33}^{T}) for each run.

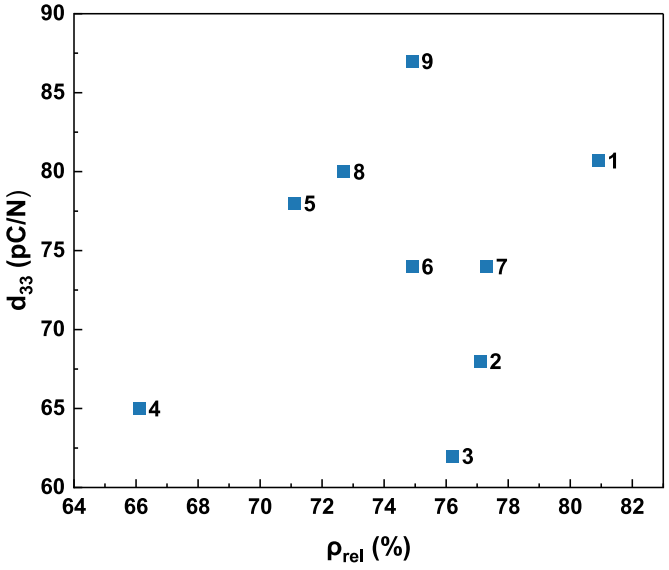

Fig. 13. d_{33} values versus relative density (ρ_{rel}) for all the runs.

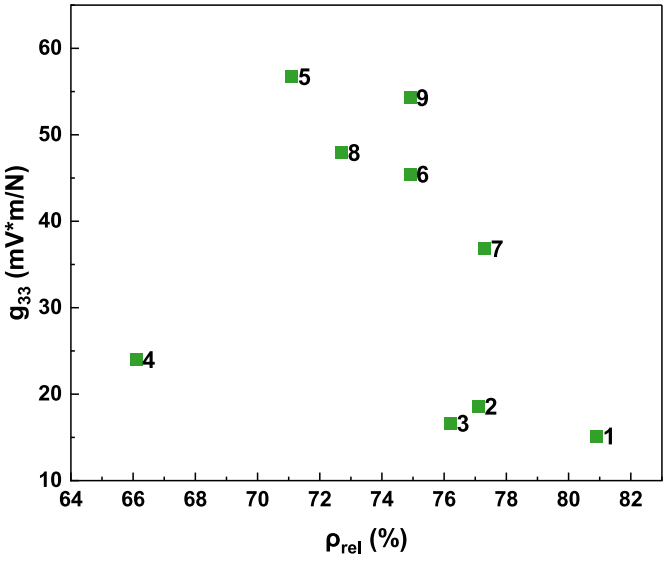

Fig. 14. g_{33} values versus relative density (ρ_{rel}) for all the runs.

would allow for the compensation of these discrepancies during CAD design and, more important, to be able to produce complex geometries with the purpose to enhance the piezoelectric properties.

To provide an adequate number of degrees of freedom for the statistical analysis, it was necessary to exclude one of the parameters from the optimisation process. Based on the partial results from the ANOVA presented in Table 5, it is evident that *BST* has a nearly negligible impact on the response, as indicated by the lowest Adjusted Sum of Squares (Adj SS). Consequently, *BST* can be eliminated from further consideration in the optimisation process.

The effects on the mean responses of standard deviations show a great influence on the drying time, followed by the target bed temperature and binder saturation (Table 6). To minimise the standard deviations, the optimal values are found to be $BS = 130\%$, $DT = 14$ s, and $TBT = 60$ °C (Fig. 6).

The confirmation run (Fig. 7a) validates these observations, yielding the lowest results for both σ_d and σ_t, respectively with values of 0.03 mm and 0.02 mm, respectively (Table 7).

In comparison to the best experimental run (Run 5), there is a slight reduction in both standard deviations, even though the printing conditions were nearly identical, with the only difference being the adjustment of the target bed temperature from 40 °C to 60 °C.

Once the optimal printing parameters were determined, more complex geometries were designed by creating a series of grids with varying wall thickness and hole dimension. However, challenges were encountered during the de-powdering process, particularly when attempting to remove loose powder from the smaller holes where it resulted unfeasible without causing damage to the specimens, as depicted in Fig. 7b.

3.1.3. Sintered samples

During sintering, the samples reduced in size due to shrinkage, which amounted on average to ~19% in the x-y directions and ~25% in the z-axis. The increased vertical shrinkage is likely attributable to the influence of gravity, promoting the densification process between layers where larger residual porosity accumulates during the printing phase. As a consequence of this shrinkage, a slight deformation of the samples occurred, causing an upward bending effect, as illustrated in Fig. 8.

This deformation could be attributed to a different gradient of porosity distribution within the sample along z-axis, to the friction between the lower surface and the plate where the samples are placed or to

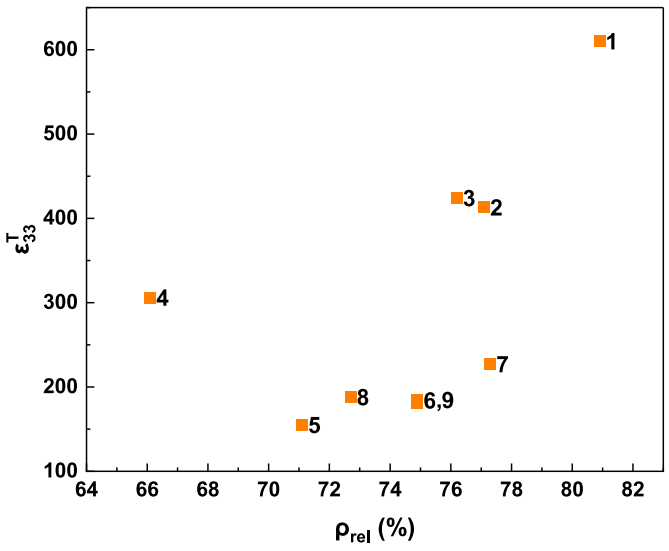

Fig. 15. ε_{33}^T values versus relative density (ρ_{rel}) for all the runs.

a temperature gradient between the upper and lower faces of the samples during the cooling step, which could be caused by differential exposure to the surrounding air and the alumina holding plate. It is noteworthy that this deformation is not uniform and varies among samples, even within the same run, suggesting that there is no clear correlation with the printing conditions employed. Moreover, the bending effect is particularly pronounced in the grid sample with the smallest wall thickness, possibly due to the increased freedom for distortion allowed by the reduced structural connectivity, as shown in Fig. 8b. Therefore, it is recommended to consider constrained sintering for components with a high surface-to-thickness ratio. Additionally, a more in-depth analysis of distortion phenomena will be addressed in further investigations.

The density values of the sintered samples are very promising, reaching a maximum value of 80.9% in Run 1 and maintaining an average of 75.0 ± 3.2% (Fig. 9). A strong dependency on print settings is evident, with the result varying by more than 10% in relative density. Maintaining a binder saturation (*BS*) of 110% yields the best results. This is likely due to the lower amount of deposited binder, which prevents the formation of more pronounced interlayer porosity that hinders densification, a phenomenon that may occur with a higher binder deposition. It should be noted, however, that runs with a *BS* of 150% do not seem to suffer from a worsening of this phenomenon compared to runs with a *BS* of 130%. Therefore, it can be assumed that, in the case of excessively high binder saturation, the additional porosity is not only dependent on the volume of the binder alone, but on the combination of the other parameters as well.

SEM analysis of the fracture surface revealed that porosities exhibited a tendency to align in a layer-by-layer fashion along the x-y plane, as depicted in Fig. 10. This alignment is likely a result of sub-optimal bed compaction, insufficient binder infiltration, and a sintering process that may not have been adequately tailored to meet the requirements of the sample's morphology. Such alignment of porosities could potentially induce an anisotropic behaviour in the sample, both in terms of mechanical and piezoelectric properties.

SEM and EDX analysis further confirmed the presence of the second phase, likely potassium niobate (KN), within the sintered samples, as indicated in Table 8. This presence of KN, already detected in the starting powder could be enhanced by alkali volatilisation, which prevents the complete transformation into the desired KNN phase. KN is distinguishable by its irregular grain morphology and is also detectable in backscattered electron configuration, exhibiting a brighter appearance on as ground surfaces, as shown in Fig. 10d. The presence of this phase may potentially have adverse effects on the final piezoelectric constants.

Throughout the densification process, the grains of stoichiometric KNN tend to grow towards a perfectly cuboidal shape. SEM images of the fracture surfaces (Fig. 11) reveal that the majority of the grains exhibit undefined polygonal shapes, with only a limited number displaying a more cuboid-like morphology. This suggests that the sintering process did not achieve the optimal level of densification.

The analysis of the piezoelectric properties shows an inverse relationship between g_{33} and ε_{33}^T, as expected by their opposite dependence on internal porosity: the first features a maximum value of 54.3 mV m N^{-1} in Run 5, while the second reaches 610 in Run 1.

It appears that d_{33} does not exhibit a linear variation with changing printing conditions, with an average value of 76 p.m. V^{-1} close to the reference one [33,37]. Fig. 12 provides a comparison of these piezoelectric properties across different experimental runs.

A possible explanation for these relationships can be linked to the number and distribution of pores [38,39]. During the heating process, the polymer present in the green bodies is removed, leaving voids that therefore depend on both the amount of added binder and its distribution. Large volumes of binder (high *BS*), especially when combined with low *DT*, result in a greater amount of interlayer liquid, leading to a marked layering of the material with concentrated interlayer porosities

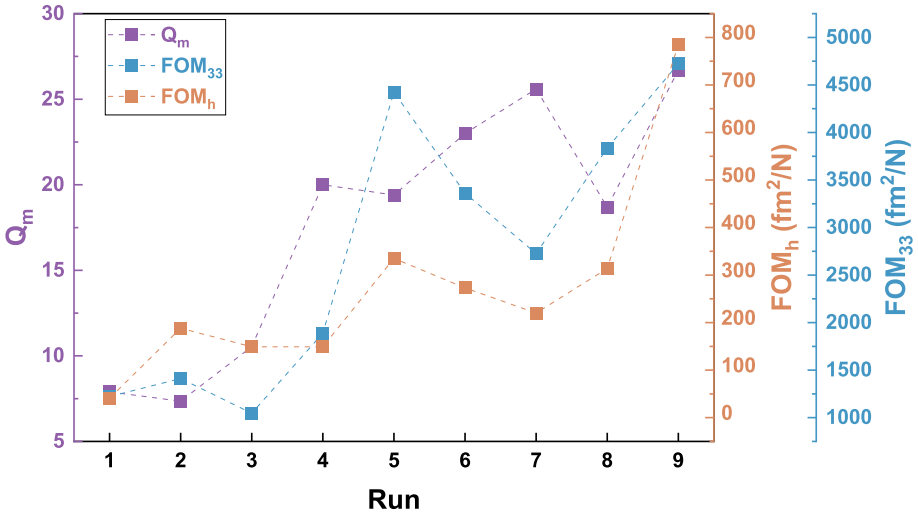

Fig. 16. Comparison of figures of merit (Q_m, FOM_{33} and FOM_h) for each run.

and reduced material connectivity in the z-direction. This seems to affect the trend in permittivity, with higher values observed in the initial runs (1–3) characterised by low *BS*, even when compared to samples with similar sintered density (e.g., run 7). Additionally, higher permittivity values are observed in Runs 4 and 7 compared to those with the same *BS*. These runs feature higher *DT* and *TBT*, resulting in longer times for liquid infiltration and enhanced evaporation, which limits the formation of interlayer porosities.

d_{33} values measured exhibit an acceptable peak value of 87 pC N^{-1} and no clear correlation to density or printing conditions (Fig. 13). This lack of correlation is likely due to the dependence of strain coefficients on additional factors, such as the effectiveness of the poling process in a heterogeneous microstructure and the presence of second phases. Porosity leads to variations in both the direction and intensity of the electric field within the material, resulting in the coexistence of unpoled and poled areas within the material, which hinders the generated strain [40–42].

g_{33} and ε^T_{33} show a more strong dependence to the density level, as expected (Fig. 14, Fig. 15). A porous material can be seen as a composite one, where the voids are made of air, which is characterized by a low level of dielectric permittivity. As a consequence as the density reduces, *g33* rises and ε^T_{33} decreases [40–42].

Three parameters have been calculated (Q_m, FOM_{33}, and FOM_h [43, 44]) to provide a preliminary assessment of the performance of the printed samples as porous piezoceramics.

The mechanical quality factor Q_m expresses "the ratio of strain in phase with stress to strain out of phase with stress in the vibrating element", or in other words, the electrical energy that is transformed to mechanical energy as opposed to that which is dissipated by heat [45]. This factor can be calculated as follow: $Q_m = f_r/(f_2 - f_1)$.

FOM_{33} and FOM_h are two important figures of merit of porous piezoceramics used to assess the direct effect and use in the marine environment (e.g., SONAR and hydrophones), respectively. The former is the product of d_{33}*g_{33} and allows us to evaluate the piezoelectric response in the direction of polarization, while the latter, also called hydrostatic FOM is the product of d_h*g_h ($d_h = d_{33} + 2d_{31}$, $g_h = d_h/(\varepsilon^T_{33}{}^*\varepsilon_0)$).

All values exhibit a trend coherent with d_{33} and g_{33}, with the mechanical quality factor and figures of merit reaching their maximum values in Run 9 (Fig. 16). In particular, FOM_{33} is important for energy harvesting in the 33 mode, since it is correlated to the stored electrical energy within a piezo-active material when stress is applied. It is worth noting that the maximum value of FOM_{33} is comparable to and even larger than, the analogous figure of merit for full-density material. This is due to the low value of the relative permittivity, which is also an important fact for other *FOMs* connected to energy harvesting.

However, it is worth noting that Q_m values are limited for all the samples, making them unsuitable for high frequencies or in-resonance applications. Nonetheless, the high FOM_s for porous piezoceramics suggest that binder jetting is a promising shaping technique for specific fields of interest, though a more comprehensive understanding of the correlation between the process, microstructure, and properties is still needed.

4. Conclusions

In this study, the primary objective was to explore the feasibility and optimisation of printing parameters using Binder Jetting (BJT) with commercial KNN powder.

For the green samples, the results revealed that an intermediate amount of binder (*BS* = 130%), when combined with adequate drying conditions (*DT* = 14 s, *TBT* = 60 °C), yielded optimal printing precision. This demonstrates the capability to produce samples with good repeatability, which is a fundamental requirement for potential industrial-scale production that, combined with the possibilities to create new geometries that are almost unfeasible with traditional manufacturing technologies, show the high potential of Binder Jetting for the production of piezoelectric devices.

Using the optimised parameters, it became possible to print grids with reduced wall thickness as low as 0.7 mm. However, challenges were encountered during the de-powdering process of thin holes. It is worth noting that an adjustment is necessary when dimensioning components in the z-direction, as the addition of binder leads to an approximate 40% oversizing of the greens in this direction. Consideration must also be given to the shrinkage during sintering, which amounts to around 19% in the x-y directions and 25% in the z-direction.

It was observed that an increase in *BS* and/or a reduction in *DT* and *TBT* resulted in apparent higher green body density due to the greater amount of binder within the specimens. The densification process, due to the high shrinkage, caused deformation of the parts, that was not associated with specific printing conditions. This deformation was particularly noticeable for grid structures with thin wall thicknesses, as their structure was less constrained. The relative density values of the sintered samples have reached excellent values, exceeding 80%.

SEM analysis indicated that the interlayer longitudinal porosity introduced by the printing process led to microstructural anisotropy, influencing the piezoelectric and mechanical properties. Most grains are far from the ideal cuboid configuration typical of KNN, underlining the influence of the undesired second phase on the microstructural development during sintering.

Acceptable values were achieved for d_{33} (87 pC N^{-1}) when compared to dense references (80–120 pC N^{-1} [12,22]) and no distinct correlation was found with the different printing parameters, nor with the final density of the parts. On the contrary, ε^T_{33} and g_{33} were found to be dependent on the internal porosity distribution, which, in turn, correlated with the control of binder deposition and infiltration during printing.

While Q_m values were modest across all runs, FOM_{33} and FOM_h showed promise and could be valuable in specific applications where customized designs are advantageous.

CRediT authorship contribution statement

Francesco Bertolini: Methodology, Formal analysis, Investigation, Data curation, Writing – original draft, Visualization. **Marco Mariani:** Conceptualization, Methodology, Validation, Writing – review & editing. **Elisa Mercadelli:** Investigation, Formal analysis. **Carlo Baldisserri:** Investigation, Formal analysis. **Carmen Galassi:** Validation, Writing – review & editing, Supervision. **Claudio Capiani:** Investigation, Formal analysis. **Raffaele Ardito:** Conceptualization, Resources, Project administration, Funding acquisition, Supervision. **Nora Lecis:** Conceptualization, Resources, Project administration, Funding acquisition, Supervision.

Declaration of competing interest

The authors declare that they have no known competing financial interests or personal relationships that could have appeared to influence the work reported in this paper.

Acknowledgements

The authors would like to acknowledge the "Functional Sintered Materials (Funtasma)" Interdepartmental Laboratory of Politecnico di Milano, where this research activity was partially developed. EM acknowledges the support from the project "DIGIMAN – Soluzioni per la DIGItalizzazione delle aziende nel settore MANifatturiero" – PG/2018/631166, in the frame of the POR FESR 2014–2020 programme of the Regione Emilia Romagna (Italy).

Moreover, the authors would like to acknowledge the support provided by STMicroelectronics.

The author Raffaele Ardito acknowledges the support of the H2020 FET-proactive project MetaVEH under grant agreement No. 952039.

References

[1] Chen C, Wang X, Wang Y, Yang D, Yao F, Zhang W, et al. Additive manufacturing of piezoelectric materials. Adv Funct Mater 2020;30:2005141. https://doi.org/10.1002/adfm.202005141.

[2] Lakhdar Y, Tuck C, Binner J, Terry A, Goodridge R. Additive manufacturing of advanced ceramic materials. Prog Mater Sci 2021;116:100736. https://doi.org/10.1016/j.pmatsci.2020.100736.

[3] Mostafaei A, Elliott AM, Barnes JE, Li F, Tan W, Cramer CL, et al. Binder jet 3D printing—process parameters, materials, properties, modeling, and challenges. Prog Mater Sci 2021;119:100707. https://doi.org/10.1016/j.pmatsci.2020.100707.

[4] Lv X, Ye F, Cheng L, Fan S, Liu Y. Binder jetting of ceramics: powders, binders, printing parameters, equipment, and post-treatment. Ceram Int 2019;45:12609–24. https://doi.org/10.1016/j.ceramint.2019.04.012.

[5] Du W, Ren X, Ma C, Pei Z. Binder jetting additive manufacturing of ceramics: a literature review. Vol. 14 emerg. Technol. Mater. Genet. To struct. Saf. Eng. Risk anal., vol. 142. American Society of Mechanical Engineers; 2017. p. 1–12. https://doi.org/10.1115/IMECE2017-70344.

[6] Ziaee M, Crane NB. Binder jetting: a review of process, materials, and methods. Addit Manuf 2019;28:781–801. https://doi.org/10.1016/j.addma.2019.05.031.

[7] Uchino K. Fundamentals of piezoelectrics. Encycl. Smart mater. Elsevier; 2022. p. 1–21. https://doi.org/10.1016/B978-0-12-803581-8.12129-0.

[8] Erturk A, Inman DJ. Piezoelectric energy harvesting. Wiley; 2011. https://doi.org/10.1002/9781119991151.

[9] Krushynska AO, Torrent D, Aragón AM, Ardito R, Bilal OR, Bonello B, et al. Emerging topics in nanophononics and elastic, acoustic, and mechanical metamaterials: an overview. Nanophotonics 2023;12:659–86. https://doi.org/10.1515/nanoph-2022-0671.

[10] De Ponti JM, Colombi A, Riva E, Ardito R, Braghin F, Corigliano A, et al. Experimental investigation of amplification, via a mechanical delay-line, in a rainbow-based metamaterial for energy harvesting. Appl Phys Lett 2020;117. https://doi.org/10.1063/5.0023544.

[11] Klocke F. Modern approaches for the production of ceramic components. J Eur Ceram Soc 1997;17:457–65. https://doi.org/10.1016/s0955-2219(96)00163-x.

[12] Li J-F, Wang K, Zhu F-Y, Cheng L-Q, Yao F-Z. (K,Na)NbO 3 -based lead-free piezoceramics: fundamental aspects, processing technologies, and remaining challenges. J Am Ceram Soc 2013;96:3677–96. https://doi.org/10.1111/jace.12715.

[13] DIRECTIVE 2002/95/EC OF THE EUROPEAN PARLIAMENT AND OF THE COUNCIL of 27 January 2003 on the restriction of the use of certain hazardous substances in electrical and electronic equipment. RoHS); 2003.

[14] DIRECTIVE 2002/96/EC OF THE EUROPEAN PARLIAMENT AND OF THE COUNCIL of 27 January 2003 on waste electrical and electronic equipment. WEEE); 2003.

[15] Ministry of Information Industry China. Measures for the administration on pollution control of electronic information products. Ministry of Information Industry China; 2006.

[16] Minister of Economy Trade and Industry, of Japan. Law for promotion of effective utilization of Resources. Minister of Economy, Trade and Industry of Japan; 2001.

[17] Ministry of Environment and Forestry Turkey. Restriction of the use of certain hazardous substances in electrical and electronic equipment. Ministry of Environment and Forestry Turkey; 2008.

[18] Produktforskriften (Product Regulations Norway). Regulations relating to restrictions on the manufacture, import, export, sale and use of chemicals and other products hazardous to health and the environment. 2004.

[19] U.S. California Senate. Solid waste: hazardous electronic waste. U.S. California Senate; 2004.

[20] Environment and Labor Committee of the National Assembly of Korea. Act for resource recycling of electrical and electronic equipment and vehicles. Environment and Labor Committee of the National Assembly of Korea; 2007.

[21] Water Hyder Consulting Pty Ltd for the Department of Environment and, Australia R. Preliminary environmental and economic assessment of Australian RoHS policy. Hyder Consulting Pty Ltd for the Department of Environment and Water Resources Australia; 2007.

[22] Wu J, Xiao D, Zhu J. Potassium–sodium niobate lead-free piezoelectric materials: past, present, and future of phase boundaries. Chem Rev 2015;115:2559–95. https://doi.org/10.1021/cr5006809.

[23] Mariani M, Beltrami R, Migliori E, Cangini L, Mercadelli E, Baldisserri C, et al. Additive manufacturing of lead-free KNN by binder jetting. J Eur Ceram Soc 2022;42:5598–605. https://doi.org/10.1016/j.jeurceramsoc.2022.05.075.

[24] Mariani M, Mercadelli E, Cangini L, Baldisserri C, Galassi C, Capiani C, et al. Additive manufacturing of piezoelectric niobium-doped lead zirconate titanate (PZT-N) by binder jetting. Crystals 2023;13:883. https://doi.org/10.3390/cryst13060883.

[25] Chavez LA, Wilburn BR, Ibave P, Delfin LC, Vargas S, Diaz H, et al. Fabrication and characterization of 3D printing induced orthotropic functional ceramics. Smart Mater Struct 2019;28:125007. https://doi.org/10.1088/1361-665X/ab4e0a.

[26] Sufiiarov V, Kantyukov A, Popovich A, Sotov A. Synthesis of spherical powder of lead-free BCZT piezoceramics and binder jetting additive manufacturing of triply periodic minimum surface lattice structures. Materials 2022;15:6289. https://doi.org/10.3390/ma15186289.

[27] Gaytan SM, Cadena MA, Karim H, Delfin D, Lin Y, Espalin D, et al. Fabrication of barium titanate by binder jetting additive manufacturing technology. Ceram Int 2015;41:6610–9. https://doi.org/10.1016/j.ceramint.2015.01.108.

[28] Schipf DR, Yesner GH, Sotelo L, Brown C, Guild MD. Barium titanate 3–3 piezoelectric composites fabricated using binder jet printing. Addit Manuf 2022;55:102804. https://doi.org/10.1016/j.addma.2022.102804.

[29] Jankovic A, Chaudhary G, Goia F. Designing the design of experiments (DOE) – an investigation on the influence of different factorial designs on the characterization of complex systems. Energy Build 2021;250. https://doi.org/10.1016/j.enbuild.2021.111298.

[30] Peace GS. Taguchi methods: a hands-on approach. Addison-Wesley; 1992.

[31] Bafaluy Ojea S, Torrents-Barrena J, Pérez Prado T, Muñoz Moreno R, Sket F. Binder Jet green parts microstructure: advanced quantitative analysis. J Mater Res Technol 2023. https://doi.org/10.1016/j.jmrt.2023.02.051.

[32] Miyanaji H, Orth M, Akbar JM, Yang L. Process development for green part printing using binder jetting additive manufacturing. Front Mech Eng 2018;13:504–12. https://doi.org/10.1007/s11465-018-0508-8.

[33] Ringgaard E, Wurlitzer T, Wolny WW. Properties of lead-free piezoceramics based on alkali niobates. Ferroelectrics 2005;319:97–107. https://doi.org/10.1080/00150190590965497.

[34] IEEE. IEEE standard on piezoelectricity: an American national standard. ANSI/IEEE Std 1988;176–1987:8–10. https://doi.org/10.1109/IEEESTD.1988.79638.

[35] Gregorsky SJ. High green density metal parts by vibrational compaction of dry powder in three dimensional printing process. Massachusetts Institute of Technology; 1996.

[36] Farzadi A, Solati-Hashjin M, Asadi-Eydivand M, Osman NAA. Effect of layer thickness and printing orientation on mechanical properties and dimensional accuracy of 3D printed porous samples for bone tissue engineering. PLoS One 2014;9:e108252. https://doi.org/10.1371/JOURNAL.PONE.0108252.

[37] Zuo R, Rodel J, Chen R, Li L. Sintering and electrical properties of lead-free Na0.5K0.5NbO3 piezoelectric ceramics. J Am Ceram Soc 2006;89. https://doi.org/10.1111/j.1551-2916.2006.00991.x. 2010–5.

[38] Banno H. Effects of porosity on dielectric, elastic and electromechanical properties of Pb(Zr, Ti)O3 ceramics with open pores: a theoretical approach. Jpn J Appl Phys 1993;32:4214–7. https://doi.org/10.1143/JJAP.32.4214.

[39] Zhang Y, Roscow J, Lewis R, Khanbareh H, Topolov VY, Xie M, et al. Understanding the effect of porosity on the polarisation-field response of ferroelectric materials. Acta Mater 2018;154:100–12. https://doi.org/10.1016/j.actamat.2018.05.007.

[40] Martínez-Ayuso G, Friswell MI, Haddad Khodaparast H, Roscow JI, Bowen CR. Electric field distribution in porous piezoelectric materials during polarization. Acta Mater 2019;173:332–41. https://doi.org/10.1016/j.actamat.2019.04.021.

[41] Rybyanets AN, Rybyanets AA. Ceramic piezocomposites: modeling, technology, and characterization. IEEE Trans Ultrason Ferroelectrics Freq Control 2011;58:1757–73. https://doi.org/10.1109/TUFFC.2011.2013.

[42] Pabst W, Hříbalová S, Uhlířová T. Quasi-laminate and quasi-columnate modeling of dielectric and piezoelectric properties of cubic-cell metamaterials. J Eur Ceram Soc 2022;42:1396–406. https://doi.org/10.1016/j.jeurceramsoc.2021.12.013.

[43] Zhang Y, Roscow J, Xie M, Bowen C. High piezoelectric sensitivity and hydrostatic figures of merit in unidirectional porous ferroelectric ceramics fabricated by freeze casting. J Eur Ceram Soc 2018;38:4203–11. https://doi.org/10.1016/j.jeurceramsoc.2018.04.067.

[44] Tichý J, Erhart J, Kittinger E, Přívratská J. Fundamentals of piezoelectric sensorics. Berlin, Heidelberg: Springer Berlin Heidelberg; 2010. https://doi.org/10.1007/978-3-540-68427-5.

[45] Turner RC, Fuierer PA, Newnham RE, Shrout TR. Materials for high temperature acoustic and vibration sensors: a review. Appl Acoust 1994;41:299–324. https://doi.org/10.1016/0003-682X(94)90091-4.